Article

Precision test of statistical dynamics with state-to-state ultracold chemistry

https://doi.org/10.1038/s41586-021-03459-6

Received: 12 January 2021

Accepted: 16 March 2021

Published online: 19 May 2021

Check for updates

Yu Liu[1,2,3,6,7]✉, Ming-Guang Hu[1,2,3,7], Matthew A. Nichols[1,2,3], Dongzheng Yang[4], Daiqian Xie[4], Hua Guo[5] & Kang-Kuen Ni[1,2,3]✉

Chemical reactions represent a class of quantum problems that challenge both the current theoretical understanding and computational capabilities[1]. Reactions that occur at ultralow temperatures provide an ideal testing ground for quantum chemistry and scattering theories, because they can be experimentally studied with unprecedented control[2], yet display dynamics that are highly complex[3]. Here we report the full product state distribution for the reaction $2KRb \rightarrow K_2 + Rb_2$. Ultracold preparation of the reactants allows us complete control over their initial quantum degrees of freedom, whereas state-resolved, coincident detection of both products enables the probability of scattering into each of the 57 allowed rotational state-pairs to be measured. Our results show an overall agreement with a state-counting model based on statistical theory[4–6], but also reveal several deviating state-pairs. In particular, we observe a strong suppression of population in the state-pair closest to the exoergicity limit as a result of the long-range potential inhibiting the escape of products. The completeness of our measurements provides a benchmark for quantum dynamics calculations beyond the current state of the art.

Chemical reactions, at the most fundamental level, are quantum mechanical processes whereby reactants are transformed into products. Consequently, a complete characterization of a reaction requires the quantum state resolution of both the reactants and the products. Over the past decade, ultracold molecules have emerged as a powerful platform for achieving complete control over the various internal degrees of freedom of the reactants[7–10]. Additionally, collisions between ultracold molecules occur with the single lowest allowed partial waves (*s*- or *p*-waves)[11]. Using these highly controlled molecules, studies of overall reaction rates have revealed the effects of long-range forces[12,13] and scattering resonances[14,15] with unprecedented resolution. However, a complete characterization of these ultracold reactions at a state-to-state level has remained challenging, with progress limited to weakly bound systems thus far[16,17], which calls for a comprehensive method for detecting the quantum state information of the reaction products.

Much of our understanding about reactivity at the quantum level is obtained through a close interaction between experiment and theory[18,19]. Ultracold reactions bring challenges to current reaction dynamics theories, and can play a critical part in the next stage of their development[2]. On the one hand, preparing reactants at ultralow temperatures can induce highly complex dynamics in reactions involving merely three or four atoms[20]. For example, recent studies of reactions between ultracold bi-alkalis revealed that the transient intermediate complexes involved can exist for millions of molecular vibrations[21,22], and exact calculations for such dynamics require computational powers beyond the state-of-the-art[1]. On the other hand, the small sizes of these systems make them conducive to complete product quantum state mapping. Such a measurement, when combined with deterministic reactant state preparation, will provide the most precise set of benchmarks for future theories.

Although the complexity of ultracold reactions hinders exact quantum calculations, statistical theories provide a viable alternative for characterizing their dynamics[4–6]. The central assumption of such theories is that the intermediate complex has sufficient time to ergodically explore the reaction phase space and redistribute its energy among the available modes of motion, leading to an equal partitioning of scattering probabilities into all allowed product channels[23]. This model has been widely used to predict the measured product state distributions of complex-forming reactions with reasonable success[24–26], although systematic deviations were found and were often attributed to insufficiently long complex lifetimes. In contrast, because of the prolonged intermediate stage of ultracold reactions, state-to-state investigations of these systems will provide rigorous tests for statistical theories[27], and allow for a critical evaluation of any non-statistical behaviour[28]. Furthermore, the precise preparation of the collision energy and partial wave in an ultracold reaction offers an opportunity to examine quantum effects in product states near the energy threshold.

In this study, we investigate the product state distribution of the exchange reaction between ultracold KRb molecules prepared in their rovibronic ground state. Using a detection scheme that combines quantum-state-selective ionization and coincidence ion imaging, we probe pairs of products (K_2 and Rb_2) that emerge from the same reaction events. In this way, we are able to measure the scattering probabilities for all allowed product rotational state-pairs, $|N_{K_2}, N_{Rb_2}\rangle$, of which there are 57 in total. The resulting distribution is quantitatively

[1]Department of Chemistry and Chemical Biology, Harvard University, Cambridge, MA, USA. [2]Department of Physics, Harvard University, Cambridge, MA, USA. [3]Harvard-MIT Center for Ultracold Atoms, Cambridge, MA, USA. [4]Institute of Theoretical and Computational Chemistry, School of Chemistry and Chemical Engineering, Nanjing University, Nanjing, China. [5]Department of Chemistry and Chemical Biology, University of New Mexico, Albuquerque, NM, USA. [6]Present address: Time and Frequency Division, National Institute of Standards and Technology, Boulder, CO, USA. [7]These authors contributed equally: Yu Liu, Ming-Guang Hu. ✉e-mail: yu.liu-1@colorado.edu; ni@chemistry.harvard.edu

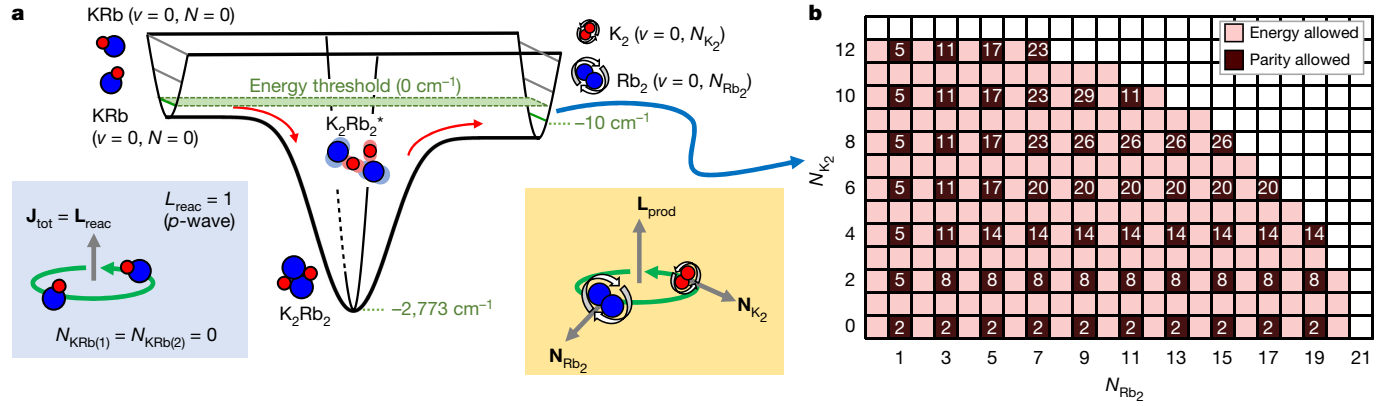

Fig. 1 | Energetics and product quantum states for ultracold reactions between KRb molecules. a, Schematic of the potential energy surface for the reaction. Reactant KRb molecules are prepared in the rovibrational ground states $|v=0, N=0\rangle$, and the K_2 and Rb_2 products emerge in states $|v=0, N_{K_2}\rangle$ and $|v=0, N_{Rb_2}\rangle$. The insets show the angular momentum vectors of the reactants and products. Two ground-state KRb molecules collide via *p*-wave collision, giving the system a total angular momentum of $J_{tot}=1$. **b**, Product rotational state-pairs and their degeneracies. The light-red-shaded region represents state-pairs that satisfy energy conservation, while the dark-red-shaded squares represent those that additionally satisfy the parity constraint imposed by the exchange statistics of identical product nuclei. The number superimposed over each allowed state-pair represents its degeneracy, which is used to construct the state-counting model.

compared to a state-counting model based on statistical theory through hypothesis testing. The test indicates good agreement between the measurement and the model for a subset containing 50 state-pairs, but reveals significant deviations in several state-pairs. In particular, a highly suppressed scattering probability is observed for the products with the lowest translational energy, which demonstrates the influence of the long-range potential on product formation.

Each experiment begins with the preparation of a dilute gas of 10^4 fermionic $^{40}K^{87}Rb$ molecules in a single hyperfine level of their absolute ground electronic, vibrational, and rotational state[29]. The molecules are confined within a crossed optical dipole trap (ODT), and have a peak density of 10^{12} cm^{-3} and a temperature of 500 nK (ref. [30]). Once prepared, the molecules undergo the exchange reaction[31]

$$\mathrm{KRb}(v_{\mathrm{KRb}}=0, N_{\mathrm{KRb}}=0) + \mathrm{KRb}(v_{\mathrm{KRb}}=0, N_{\mathrm{KRb}}=0) \rightarrow \mathrm{K_2Rb_2^*} \rightarrow \mathrm{K_2}(v_{\mathrm{K_2}}=0, N_{\mathrm{K_2}}) + \mathrm{Rb_2}(v_{\mathrm{Rb_2}}=0, N_{\mathrm{Rb_2}}). \quad (1)$$

Here, v_s and N_s are the quantum numbers associated with the vibrational and rotational degrees of freedom of species s, respectively. Vibrations of the products are energetically restricted to their ground states, $v_{K_2}=0$ and $v_{Rb_2}=0$ (ref. [32]). The energetics of this reaction are schematically illustrated in Fig. 1a[33,34]. The deep potential well (about 2,773 cm^{-1}) and the comparatively small reaction exoergicity (about 10 cm^{-1}), combined with the ultracold preparation of the reactants, give rise to a strong bottleneck effect for the dissociation of the $K_2Rb_2^*$ complex into products. This leads to a long complex lifetime of 360 ns (ref. [21]), which provides favourable conditions for the complex to ergodically explore the reaction phase space and redistribute its energy statistically among all available modes before its dissociation.

Because reaction (1) produces more than one molecular species, a complete characterization of its outcome requires knowledge of the population in joint quantum states of both products[35], which we label as $|N_{K_2}, N_{Rb_2}\rangle$. A given state-pair is allowed if it satisfies the conservation of energy, $|\Delta E| = U(N_{K_2}, N_{Rb_2}) + T(N_{K_2}, N_{Rb_2})$, where ΔE represents the exoergicity of the reaction, while U and T are the internal and translational energies for the state-pair, respectively. Given the literature value for $|\Delta E|$ (about 10 cm^{-1}) as well as the rotational constants of K_2 and Rb_2 (Methods), energy conservation permits a total of over 200 state-pairs, as represented by the light-red-shaded area in Fig. 1b. Further constraints are imposed by the exchange statistics of the identical nuclei within each product, which restricts the allowed states to 57 pairs wherein N_{K_2} takes on even values and N_{Rb_2} takes on odd values[32], as indicated by the dark-red-shaded squares in Fig. 1b.

Within a given state-pair, additional scattering channels arise owing to the relation between the various angular momentum vectors possessed by the products. These include the rotational angular momentum of each product species, $\mathbf{N}_{K_2}$ and $\mathbf{N}_{Rb_2}$, as well as the orbital angular momentum of their relative motion, $\mathbf{L}_{prod}$ (Fig. 1a insets). Each scattering channel is associated with a unique set of orientations of these three vectors, which, under the assumption of total angular momentum conservation, must satisfy $\mathbf{N}_{K_2} + \mathbf{N}_{Rb_2} + \mathbf{L}_{prod} = \mathbf{J}_{tot}$. Here, the quantum number for the total angular momentum of the system, J_{tot}, takes on a value of precisely 1 owing to the fact that the reactant KRb molecules ($N_{KRb}=0$) are fermionic and are therefore restricted to collide via *p*-wave collisions at ultralow temperatures[11]. While the scattering channels associated with a given state-pair are effectively degenerate in energy and are unresolved by our detection (Methods), each represents a possible exit channel for the products, and therefore possesses an equal scattering probability under the assumption that the system behaves statistically. Thus, we construct a statistical model for the product state distribution in terms of the scattering probabilities into various state-pairs, as follows: $P^0_{sc}(N_{K_2}, N_{Rb_2}) = \mathcal{D}_{N_{K_2},N_{Rb_2}} / \sum_{\mathcal{S}} \mathcal{D}_{N_{K_2},N_{Rb_2}}$, which we refer to as the state-counting model. Here, $\mathcal{D}_{N_{K_2},N_{Rb_2}}$ represents the number of channels associated with a given state-pair (Fig. 1b), that is, its degeneracy, and is counted using a set of triangle inequalities for the quantum numbers associated with the product angular momentum vectors (Methods). $\mathcal{S}$ here represents the complete set of allowed state-pairs whose exact members are determined by our measurements.

To probe the population in a given product state-pair, we developed a scheme that combines state-resolved product sampling[36] with coincidence detection[37,38] (Fig. 2a), and which involves three main steps: simultaneous ionization of K_2 and Rb_2 from select quantum states via laser pulses, velocity-map imaging of the resulting ions, and determination of the number of K_2^+ and Rb_2^+ ion pairs that are associated with the same reaction events. We focus our discussions here on the third step, as details of the first two steps can be found in refs. [30,32] and Methods. Each simultaneous observation of a K_2^+ ion and a Rb_2^+ ion represents a possible detection of products generated by the same event in the target state-pair $|N_{K_2}, N_{Rb_2}\rangle$ – a coincident count. Such an observation, however, could also be due to products generated by separate reactions—an accidental count. To identify the coincident counts, we utilize the fact that products from the same event must

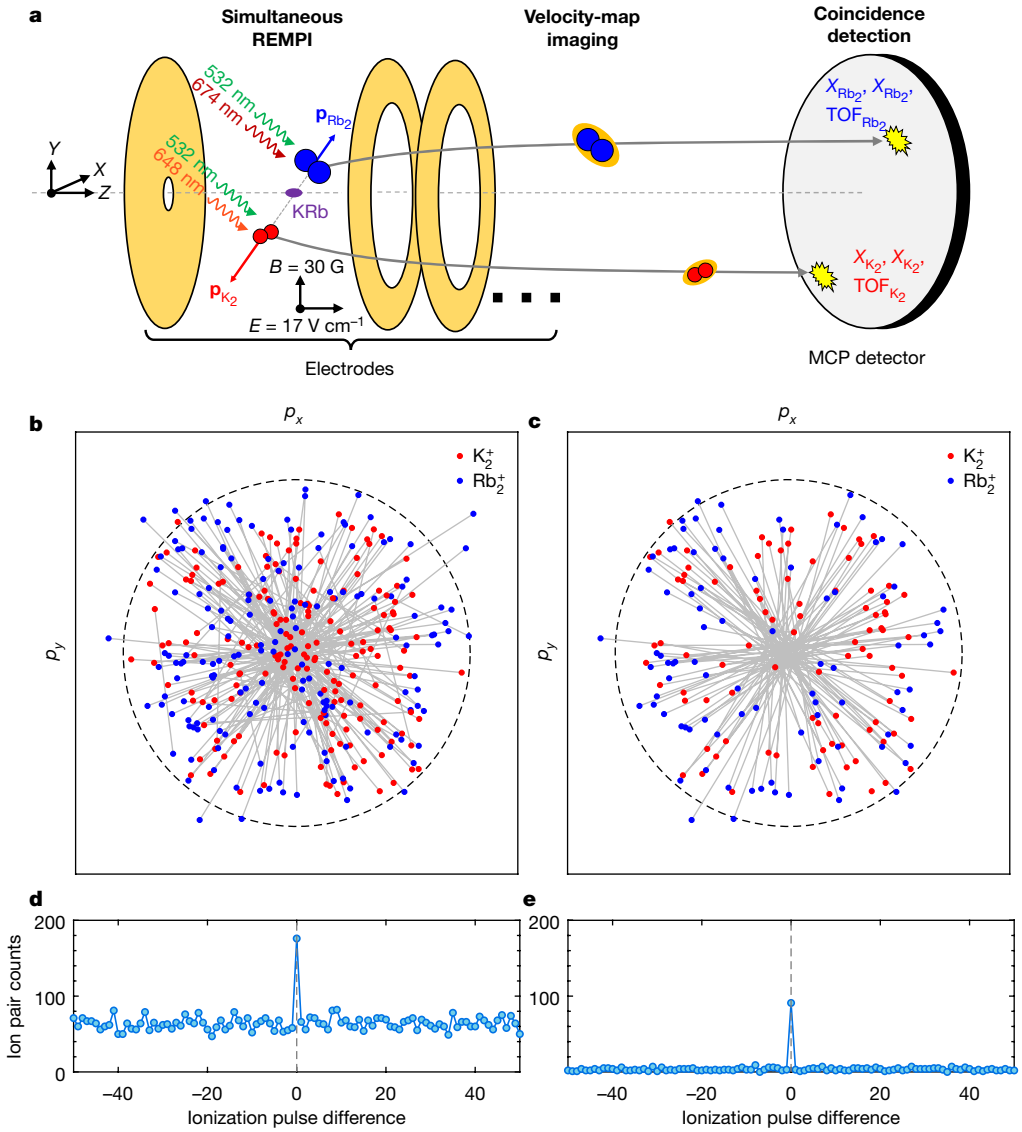

Fig. 2 | State-resolved coincidence detection of reaction products. **a**, Schematic of the ionization and detection process. Products in rotational states N_{K_2} and N_{Rb_2} are simultaneously ionized via resonance-enhanced multiphoton ionization (REMPI) pulses. The resulting ions are then velocity-map-imaged onto a microchannel plate (MCP) detector. The position and TOF of the ions are recorded and used to screen for coincidence counts. We apply a 17 V cm^{-1} electric field (E) for ion extraction and a 30 G magnetic field (B) for maintaining the nuclear spin quantization. **b**, Momentum image of simultaneously detected K_2^+ and Rb_2^+ ions associated with the states $N_{K_2} = 6$ and $N_{Rb_2} = 7$. Each simultaneously detected ion pair is connected by a line. This image is derived from the raw image of ion impact positions via the position–momentum relations described in Methods. The dashed circle corresponds to the maximum achievable transverse momentum for products in $|6, 7\rangle$. **c**, Momentum image of the coincident product ion pairs, obtained by screening for the ion pairs in **b**, that satisfy momentum conservation. **d**, The number of K_2^+–Rb_2^+ pairs as a function of the number of ionization pulses by which their detections are separated. Zero on the horizontal axis corresponds to simultaneous counts, which contains both correlated (coincident) and uncorrelated (accidental) ions, while a non-zero difference corresponds to ions that are generated by separate pulses, and are therefore uncorrelated. **e**, A plot similar to **d**, but with the uncorrelated counts screened out.

satisfy the conservation of linear momentum, $\mathbf{p}_{K_2} + \mathbf{p}_{Rb_2} = 0$, while those that are from separate events are uncorrelated, and are therefore not bound by this constraint. In our system, the momentum components transverse to the time-of-flight (TOF) axis are mapped to spatial positions on an ion detector through velocity-map imaging, while the component along this axis is encoded in the ion TOF (Methods). To illustrate this screening process, Fig. 2b shows an image of all simultaneous ion pairs for the state-pair $|6, 7\rangle$, while Fig. 2c highlights those that satisfy momentum conservation and are considered to be from the same reaction events. We assess the efficacy of this process by applying it to detected K_2^+ and Rb_2^+ that are ionized by different laser pulses, and must therefore be uncorrelated (Methods). Figure 2d, e displays the number of K_2^+–Rb_2^+ pairs before and after screening, respectively, as a function of the difference in the pulse number, demonstrating that the uncorrelated counts are effectively screened away.

Using this coincidence detection scheme, we observe coincidence signals for all state-pairs with internal energies less than or equal to that of $|12, 7\rangle$ ($U = 9.77$ cm^{-1}). The next state pair that is higher in energy, $|10, 13\rangle$ ($U = 10.01$ cm^{-1}), shows a signal that is consistent with zero. This allows us to determine the complete set of allowed state-pairs, $\mathcal{S}$, which contains 57 total members. Figure 3a shows the measured product state distribution, defined as the observed probabilities of scattering into the various state-pairs: $P_{sc}^{meas}(N_{K_2}, N_{Rb_2}) = \mathcal{N}_{N_{K_2}, N_{Rb_2}} / \sum_{\mathcal{S}} \mathcal{N}_{N_{K_2}, N_{Rb_2}}$. Here, $\mathcal{N}_{N_{K_2}, N_{Rb_2}}$ represents the normalized coincident counts for a given state-pair, which are obtained through a normalization of the raw coincident counts by the number of experimental cycles, fluctuations in

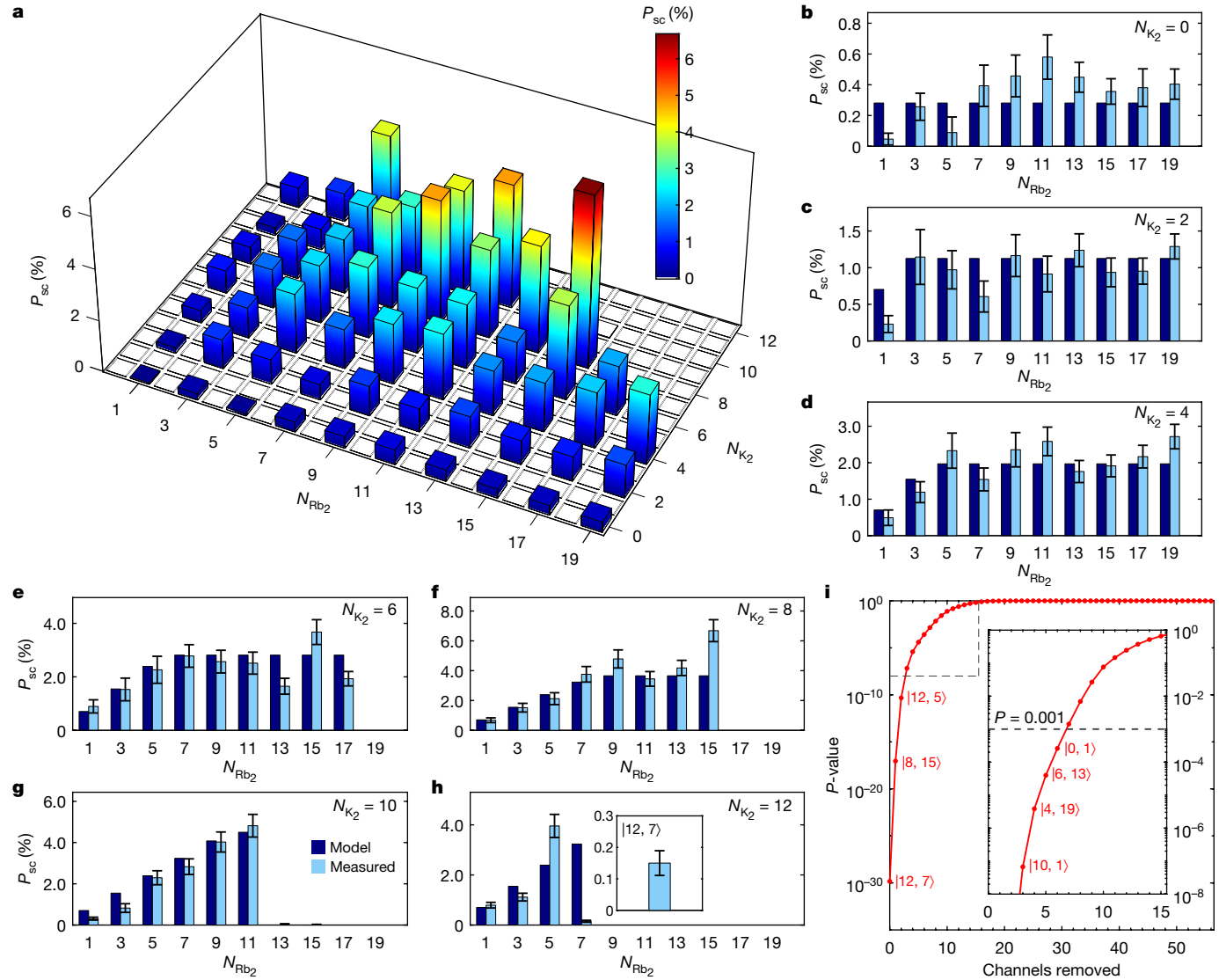

Fig. 3 | Measured product state distribution and comparison to statistical theory. a, Measured scattering probability into various product state-pairs $|N_{K_2}, N_{Rb_2}\rangle$. **b**–**h**, Comparing the measured (P_{sc}^{meas}) scattering probabilities to predictions (P_{sc}^{0}) from the state-counting model. Each frame displays the probabilities for state-pairs with a particular value of N_{K_2} as a function of their N_{Rb_2}. The error bar for each measurement includes shot noise as well as 11% relative fluctuations in experimental conditions. The state-pairs $|10, 13\rangle$ and $|10, 15\rangle$ are energetically forbidden to be populated, and have measured populations that are consistent with zero. The inset of **h** shows a close-up view of the scattering probability for the state-pair $|12, 7\rangle$, which displays a strongly suppressed population compared to the prediction. **i**, The *P*-value for the hypothesis that the measured and model distributions agree, as state-pairs that deviate most significantly from the prediction (labelled in the figure) are successively removed. An 11% relative fluctuation in experimental conditions was considered for this calculation (Methods). The inset to **i** shows a close-up of the boxed region. The dashed line indicates $P = 0.001$, a threshold below which the hypothesis should be rejected.

experimental conditions, and the product-velocity-dependent efficiencies of our ionization sampling (Methods). The results demonstrate, in general, enhanced scattering probability for state-pairs that have both large and closely matching values of N_{K_2} and N_{Rb_2} (for example, $|10, 11\rangle$), while scattering into state-pairs with small N_{K_2} or N_{Rb_2} is disfavoured.

We compare the measured product state distribution to the state-counting model (P_{sc}^{0}) in Fig. 3b–h. Each measurement is assigned an error bar of $\pm\delta P_{sc}^{meas}$, which represents the measurement uncertainty that arises primarily from the Poissonian statistics of the coincidence ion counting as well as fluctuations in experimental conditions (Methods). We quantify the degree to which the measured and predicted distributions agree using the likelihood ratio test[39]. Specifically, we test the hypothesis that the observation matches our model, as state-pairs that deviate most significantly from the predictions are successively removed from the test (Methods). For each new subset of state-pairs, the *P*-value for the hypothesis is calculated to characterize its statistical significance. The results, displayed in Fig. 3i, show that the threshold of $P = 0.001$, above which the hypothesis cannot be rejected, is reached after the removal of 7 state-pairs (labelled in Fig. 3). Thus, for a subset that contains the majority of the allowed state-pairs, we find the measured outcome to be consistent with the model. Since all reactants are prepared in a single quantum state, such an outcome cannot be attributed to any ensemble averaging effect, but must be due to the intrinsic dynamics of the reaction.

Because of the precise control over the collision energy, our experiment is sensitive to effects of the long-range potential on product formation in near-threshold states. In particular, we observe a highly suppressed scattering probability into the state-pair $|12, 7\rangle$, which we attribute to centrifugal barriers impeding the formation of low

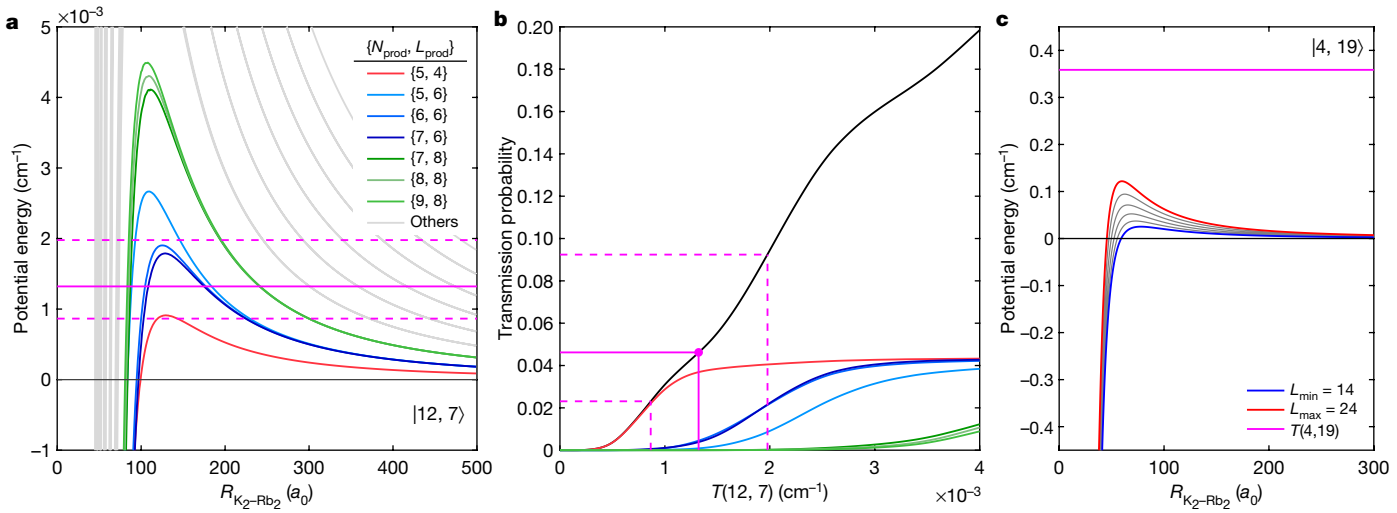

Fig. 4 | Influence of the long-range potential on product formation near the energy threshold. a, Ab initio effective long-range potentials for different scattering channels belonging to the state-pair $|12, 7\rangle$. $R_{K_2-Rb_2}$ is the distance between the product pair; a_0 is the Bohr radius. Each channel is defined by the quantum numbers N_{prod} and L_{prod} associated with the coupled rotational ($\mathbf{N}_{prod} = \mathbf{N}_{K_2} + \mathbf{N}_{Rb_2}$) and orbital ($\mathbf{L}_{prod}$) angular momenta of the products, respectively. **b**, Total transmission probability (black curve) through the centrifugal barriers and its contributions from different channels (curves of other colours) as functions of the translational energy of $|12, 7\rangle$. The colour-coding scheme follows that of **a**. The maximum contribution of each channel is given by the inverse of the degeneracy of this state-pair, 1/23 = 0.0435, and is reached when the translational energy increases sufficiently above the corresponding barrier height. We use the ratio between the measured and predicted scattering probabilities (Fig. 3h), 0.046, as an estimate for the transmission probability, and allow variations of +0.046 and −0.023 to account for uncertainties in the population before barrier transmission. This corresponds to a translational energy of $1.3^{+0.7}_{-0.5} \times 10^{-3}$ cm^{-1} (magenta lines). This value is also indicated in **a**. **c**, Potentials for the state-pair $|4, 19\rangle$. The magenta line indicates the corresponding translational energy, which is calculated based on the reaction exoergicity determined in this study. L_{min} and L_{max}, respectively, represent the minimum and maximum allowed orbital angular momentum for this state-pair.

translational energy products in this state-pair. Such an effect is beyond the state-counting model, which implicitly assumes a unit probability for product escape. To characterize this effect, we calculated the effective long-range potentials associated with the different scattering channels of $|12, 7\rangle$ (Fig. 4a), as well as the probability of products being transmitted through the associated centrifugal barriers as a function of the total translational energy, $T(12, 7)$ (Fig. 4b) (Methods). Under the assumption that the population before transmission is close to that given by the state-counting model, we use the ratio between the measured and predicted scattering probabilities, 0.046, as an estimate for the transmission probability. To this value, we assign conservative uncertainties of +0.046 and −0.023 to account for possible deviations in the pre-transmission population caused by any non-statistical effects. Comparing $0.046^{+0.046}_{-0.023}$ against the curve in Fig. 4b, we find the translational energy of this state-pair to be $T(12, 7) = 1.3^{+0.7}_{-0.5} \times 10^{-3}$ cm^{-1}. At such an energy, the orbital motion of the products is predominantly characterized by the single lowest allowed partial wave for $|12, 7\rangle$, the g-wave ($L_{prod} = 4$). This minute energy scale could enable the control of product formation via external fields[27,40], thereby extending this exceptional controllability over ultracold reactants to products. Using the newly determined translational energy and the known internal energy of $|12, 7\rangle$, we calculate the reaction exoergicity to be $|\Delta E| = T(12, 7) + U(12, 7) = 9.7711^{+0.0007}_{-0.0005}$ cm^{-1}. To the best of our knowledge, this represents the most precise determination of an exoergicity for any bimolecular chemical reaction. We note that the uncertainty in the exoergicity is dominated by that of $T(12, 7)$, since $U(12, 7)$ is derived from the precisely measured molecular constants for K_2 (ref. [41]) and Rb_2 (ref. [42]) to be accurate to within 1×10^{-4} cm^{-1} (Methods).

The breakdown of the state-counting model for the nearest-threshold state-pair highlights the importance of considering the escape process for the products. To this end, we calculate the product escape probabilities for the remaining 56 state-pairs by explicitly following their dynamics over the full-dimensional long-range potential[43] (Methods). The results show near unit probabilities (>0.999) for all 56, indicating a lack of any barriers or bottlenecks that impede product formation in these states. In particular, based on the newly determined exoergicity, the translational energies for these state-pairs far exceed the heights of the associated centrifugal barriers. This is illustrated in Fig. 4c for the second-nearest-threshold state-pair, $|4, 19\rangle$. The overall absence of long-range effects on the products implies that the deviations observed in other state-pairs (for example, $|8, 15\rangle$ and $|12, 5\rangle$) may originate from non-statistical dynamics[28], a definitive explanation for which will require exact quantum scattering calculations beyond the current state of the art.

Whereas the reactants used in the present study were prepared in their absolute ground states, our molecular state preparation can readily be extended to initialize the reactants in arbitrary rotational and vibrational states, or even superposition states with controllable relative phases. By further combining the ability to measure product quantum state information in a pair-correlated fashion, as we have demonstrated here, ultracold molecules represent a promising platform with which to advance our understanding of reaction dynamics[44,45], and to realize state-to-state control of chemical reactions. This control may be leveraged to engineer correlations between the states of product molecules emerging from a single reaction, potentially leading to a method for generating quantum entangled particles.

Online content

Any methods, additional references, Nature Research reporting summaries, source data, extended data, supplementary information, acknowledgements, peer review information; details of author contributions and competing interests; and statements of data and code availability are available at https://doi.org/10.1038/s41586-021-03459-6.

1. Li, J., Zhao, B., Xie, D. & Guo, H. Advances and new challenges to bimolecular reaction dynamics theory. *J. Phys. Chem. Lett.* **11**, 8844–8860 (2020).

2. Quéméner, G. & Julienne, P. S. Ultracold molecules under control! *Chem. Rev.* **112**, 4949–5011 (2012).
3. Croft, J. et al. Universality and chaoticity in ultracold K + KRb chemical reactions. *Nat. Commun.* **8**, 15897 (2017).
4. Light, J. C. Statistical theory of bimolecular exchange reactions. *Discuss. Faraday Soc.* **44**, 14–29 (1967).
5. Nikitin, E. E. & Umanskii, S. Y. *Theory of Slow Atomic Collisions* Vol. 30 (Springer Science & Business Media, 2012).
6. Pechukas, P. in *Dynamics of Molecular Collisions* 269–322 (Springer, 1976).
7. Julienne, P. S. Ultracold molecules from ultracold atoms: a case study with the KRb molecule. *Faraday Discuss.* **142**, 361–388 (2009).
8. Balakrishnan, N. Ultracold molecules and the dawn of cold controlled chemistry. *J. Chem. Phys.* **145**, 150901 (2016).
9. Tarbutt, M. R. Laser cooling of molecules. *Contemp. Phys.* **59**, 356–376 (2018).
10. Toscano, J., Lewandowski, H. & Heazlewood, B. R. Cold and controlled chemical reaction dynamics. *Phys. Chem. Chem. Phys.* **22**, 9180–9194 (2020).
11. Ospelkaus, S. et al. Quantum-state controlled chemical reactions of ultracold potassium-rubidium molecules. *Science* **327**, 853–857 (2010).
12. Ni, K.-K. et al. Dipolar collisions of polar molecules in the quantum regime. *Nature* **464**, 1324 (2010).
13. Guo, M. et al. Dipolar collisions of ultracold ground-state bosonic molecules. *Phys. Rev. X* **8**, 041044 (2018).
14. Yang, H. et al. Observation of magnetically tunable Feshbach resonances in ultracold $^{23}Na^{40}K + ^{40}K$ collisions. *Science* **363**, 261–264 (2019).
15. de Jongh, T. et al. Imaging the onset of the resonance regime in low-energy NO-He collisions. *Science* **368**, 626–630 (2020).
16. Rui, J. et al. Controlled state-to-state atom-exchange reaction in an ultracold atom–dimer mixture. *Nat. Phys.* **13**, 699 (2017).
17. Wolf, J. et al. State-to-state chemistry for three-body recombination in an ultracold rubidium gas. *Science* **358**, 921–924 (2017).
18. Yang, X. State-to-state dynamics of elementary bimolecular reactions. *Annu. Rev. Phys. Chem.* **58**, 433–459 (2007).
19. Clary, D. C. Theoretical studies on bimolecular reaction dynamics. *Proc. Natl Acad. Sci. USA* **105**, 12649–12653 (2008).
20. Croft, J. F. & Bohn, J. L. Long-lived complexes and chaos in ultracold molecular collisions. *Phys. Rev. A* **89**, 012714 (2014).
21. Liu, Y. et al. Photo-excitation of long-lived transient intermediates in ultracold reactions. *Nat. Phys.* **16**, 1132–1136 (2020).
22. Gregory, P. D., Blackmore, J. A., Bromley, S. L. & Cornish, S. L. Loss of ultracold $^{87}Rb^{123}Cs$ molecules via optical excitation of long-lived two-body collision complexes. *Phys. Rev. Lett.* **124**, 163402 (2020).
23. Bonnet, L. & Rayez, J. C. Some key factors of energy distributions in the products of complex-forming elementary reactions. *Phys. Chem. Chem. Phys.* **1**, 2383–2400 (1999).
24. Balucani, N. et al. Experimental and theoretical differential cross sections for the $N(^2D) + H_2$ reaction. *J. Phys. Chem. A* **110**, 817–829 (2006).
25. Sun, Z. et al. State-to-state dynamics of $H + O_2$ reaction, evidence for nonstatistical behavior. *J. Am. Chem. Soc.* **130**, 14962–14963 (2008).
26. Rivero-Santamaría, A. et al. The $O(^1D) + H_2$ ($X^1\Sigma^+$, v, j) → OH ($X^2\Pi$, v', j') + $H(^2S)$ reaction at low collision energy: when a simple statistical description of the dynamics works. *Phys. Chem. Chem. Phys.* **13**, 8136–8139 (2011).
27. González-Martínez, M. L., Dulieu, O., Larrégaray, P. & Bonnet, L. Statistical product distributions for ultracold reactions in external fields. *Phys. Rev. A* **90**, 052716 (2014).
28. Nesbitt, D. J. Toward state-to-state dynamics in ultracold collisions: lessons from high-resolution spectroscopy of weakly bound molecular complexes. *Chem. Rev.* **112**, 5062–5072 (2012).
29. Ni, K.-K. et al. A high phase-space-density gas of polar molecules. *Science* **322**, 231–235 (2008).
30. Liu, Y., Grimes, D. D., Hu, M.-G. & Ni, K.-K. Probing ultracold chemistry using ion spectrometry. *Phys. Chem. Chem. Phys.* **22**, 4861–4874 (2020).
31. Hu, M.-G. et al. Direct observation of bimolecular reactions of ultracold KRb molecules. *Science* **366**, 1111–1115 (2019).
32. Hu, M.-G. et al. Nuclear spin conservation enables state-to-state control of ultracold molecular reactions. *Nat. Chem.* https://doi.org/10.1038/s41557-020-00610-0 (2020).
33. Byrd, J. N., Montgomery, J. A. Jr & Côté, R. Structure and thermochemistry of K_2Rb, KRb_2, and K_2Rb_2. *Phys. Rev. A* **82**, 010502 (2010).
34. Yang, D. et al. A global full-dimensional potential energy surface for the K_2Rb_2 complex and its lifetime. *J. Phys. Chem. Lett.* **11**, 2605–2610 (2020).
35. Liu, K. Product pair correlation in bimolecular reactions. *Phys. Chem. Chem. Phys.* **9**, 17–30 (2007).
36. Brouard, M., O'Keeffe, P. & Vallance, C. Product state resolved dynamics of elementary reactions. *J. Phys. Chem. A* **106**, 3629–3641 (2002).
37. Continetti, R. E. Coincidence spectroscopy. *Annu. Rev. Phys. Chem.* **52**, 165–192 (2001).
38. Lee, S. K. et al. Coincidence ion imaging with a fast frame camera. *Rev. Sci. Instrum.* **85**, 123303 (2014).
39. Wasserman, L. *All Of Statistics: A Concise Course In Statistical Inference* (Springer, 2004).
40. Meyer, E. R. & Bohn, J. L. Product-state control of bi-alkali-metal chemical reactions. *Phys. Rev. A* **82**, 042707 (2010).
41. Amiot, C., Vergès, J. & Fellows, C. E.The long-range potential of the K_2 $X^1\Sigma_g^+$ ground electronic state up to 15 Å. *J. Chem. Phys.* **103**, 3350–3356 (1995).
42. Seto, J. Y., Le Roy, R. J., Verges, J. & Amiot, C. Direct potential fit analysis of the $X^1\Sigma_g^+$ state of Rb_2: nothing else will do! *J. Chem. Phys.* **113**, 3067–3076 (2000).
43. Yang, D., Huang, J., Hu, X., Xie, D. & Guo, H. Statistical quantum mechanical approach to diatom–diatom capture dynamics and application to ultracold KRb + KRb reaction. *J. Chem. Phys.* **152**, 241103 (2020).
44. Brumer, P., Bergmann, K. & Shapiro, M. Identical collision partners in the coherent control of bimolecular reactions. *J. Chem. Phys.* **113**, 2053–2055 (2000).
45. Kendrick, B., Hazra, J. & Balakrishnan, N. The geometric phase controls ultracold chemistry. *Nat. Commun.* **6**, 7918 (2015).

Methods

Reaction exoergicity from the literature

Knowledge of the reaction exoergicity, ΔE, is important for our initial determination of the allowed rovibrational states of the products and their translational energies. To this end, we calculate it using known molecular dissociation energies, as

$$\Delta E = D_0(\mathrm{K_2}) + D_0(\mathrm{Rb_2}) - 2D_0(\mathrm{KRb}). \quad (2)$$

Here, D_0 represents the dissociation energy, which is measured from the rovibrational ground state of each species to the threshold of its dissociation into two free atoms. In the case of ^{40}K^{87}Rb, Ni et al.[29] obtained D_0 from the frequency difference between the lasers used to drive a molecular Raman transition, which were calibrated using a frequency comb to megahertz-level precision. In the cases of K_2 and Rb_2, large numbers of rovibronic transition frequencies were measured and used to fit the ground electronic potentials, yielding values for the well depth, D_e, that are accurate to better than 0.1 cm^{-1}. These fitted potentials allow for the calculation of the harmonic frequencies, ω_0. The dissociation energies of K_2 and Rb_2 are then obtained by adding the zero-point-energy to the well depth, that is, $D_0 = D_e + \omega_0/2$. The best known literature values for D_e, ω_0, and D_0 are summarized in Extended Data Table 1, along with their references.

Using the tabulated values for D_0 and equation (2), we calculate an exoergicity of $\Delta E = -9.53(7)$ cm^{-1}. We note that this is lower in absolute value compared to the assumed −10.4(4) cm^{-1} calculated in ref. [11], which used an earlier literature value for $D_0(Rb_2)$ (ref. [47]). As such, we use $\Delta E \approx -10$ cm^{-1} as a rough initial estimate.

Internal energy of a state-pair

The internal energy of a product pair $|N_{K_2}, N_{Rb_2}\rangle$ in the vibrational ground state ($|v_{K_2} = 0, v_{Rb_2} = 0\rangle$) is given by

$$\begin{aligned} U(N_{K_2}, N_{Rb_2}) = {} & B_{K_2} N_{K_2}(N_{K_2}+1) - D_{K_2}(N_{K_2}(N_{K_2}+1))^2 \\ & + B_{Rb_2} N_{Rb_2}(N_{Rb_2}+1) - D_{Rb_2}(N_{Rb_2}(N_{Rb_2}+1))^2. \end{aligned} \quad (3)$$

Here, B and D are the rotational and centrifugal distortion constants, respectively. The best known literature values for B and D are listed in Extended Data Table 2, along with their references. Note that they are scaled by mass from the values measured for their more abundant isotopic counterparts, according to $B_b = B_a(\mu_a/\mu_b)$ and $D_b = D_a(\mu_a/\mu_b)^2$. Here, μ represents the reduced mass, a represents $^{85}Rb_2$ or $^{39}K_2$, b represents $^{87}Rb_2$ or $^{40}K_2$. The internal energies for all state-pairs relevant to this study are listed in Extended Data Table 3.

Counting the number of scattering channels within a state-pair

For a given state-pair $|N_{K_2}, N_{Rb_2}\rangle$, additional scattering channels arise due to the freedom in choosing the relative orientations of the corresponding rotation vectors $\mathbf{N}_{K_2}$ and $\mathbf{N}_{Rb_2}$. The number of such channels can be determined with the assumption of total angular momentum conservation throughout the reaction

$$\mathbf{J}_{\mathrm{tot}} = \mathbf{N}_{\mathrm{reac}} + \mathbf{L}_{\mathrm{reac}} = \mathbf{N}_{\mathrm{prod}} + \mathbf{L}_{\mathrm{prod}}, \quad (4)$$

where

$$\begin{aligned} \mathbf{N}_{\mathrm{reac}} &= \mathbf{N}_{\mathrm{KRb(1)}} + \mathbf{N}_{\mathrm{KRb(2)}} \\ \mathbf{N}_{\mathrm{prod}} &= \mathbf{N}_{K_2} + \mathbf{N}_{Rb_2}. \end{aligned} \quad (5)$$

Here, $\mathbf{J}_{\mathrm{tot}}$ represents the total angular momentum of the system, $\mathbf{N}_{\mathrm{reac}}$ ($\mathbf{N}_{\mathrm{prod}}$) represents the coupled rotational angular momentum of the reactants (products), and $\mathbf{L}_{\mathrm{reac}}$ ($\mathbf{L}_{\mathrm{prod}}$) represents the orbital angular momentum of the reactants (products). The above relations between angular momentum vectors are equivalent to a set of triangle inequalities on the corresponding quantum numbers, written as

$$\begin{aligned} |N_{\mathrm{KRb(1)}} - N_{\mathrm{KRb(2)}}| \le N_{\mathrm{reac}} \le |N_{\mathrm{KRb(1)}} + N_{\mathrm{KRb(2)}}|, \\ |N_{K_2} - N_{Rb_2}| \le N_{\mathrm{prod}} \le |N_{K_2} + N_{Rb_2}|, \\ |N_{\mathrm{reac}} - L_{\mathrm{reac}}| \le J_{\mathrm{tot}} \le |N_{\mathrm{reac}} + L_{\mathrm{reac}}|, \\ |L_{\mathrm{prod}} - N_{\mathrm{prod}}| \le J_{\mathrm{tot}} \le |L_{\mathrm{prod}} + N_{\mathrm{prod}}|. \end{aligned} \quad (6)$$

Owing to the presence of a 30 G magnetic field during the reaction (Fig. 2a), an additional constraint on the product angular momentum quantum numbers is imposed by the conservation of total parity[27]

$$(-1)^{N_{\mathrm{KRb(1)}}}(-1)^{N_{\mathrm{KRb(2)}}}(-1)^{L_{\mathrm{reac}}} = (-1)^{N_{K_2}}(-1)^{N_{Rb_2}}(-1)^{L_{\mathrm{prod}}}. \quad (7)$$

Because the KRb reactants in our experiments are prepared in their rovibrational ground state and collide via p-wave collisions, we have $N_{\mathrm{KRb(1)}} = N_{\mathrm{KRb(2)}} = 0$, and therefore $J_{\mathrm{tot}} = L_{\mathrm{reac}} = 1$. Given this initial condition, we count, for each given pair of $|N_{K_2}, N_{Rb_2}\rangle$, the number of $|N_{\mathrm{prod}}, L_{\mathrm{prod}}\rangle$ combinations that satisfy equations (6) and (7) to obtain its degeneracy ($\mathcal{D}$). The results are documented in Extended Data Table 3. As an example, for the state $|N_{K_2} = 2, N_{Rb_2} = 1\rangle$ there exist five channels, which are $|N_{\mathrm{prod}}, L_{\mathrm{prod}}\rangle = |1, 0\rangle$, $|1, 2\rangle$, $|2, 2\rangle$, $|3, 2\rangle$ and $|3, 4\rangle$. Note that the nuclear spins and their associated angular momenta are ignored for the purpose of this state-counting. This is justified by the results of our previous work, in which it was shown that the nuclear spins remain unchanged throughout the reaction, and are therefore effectively decoupled from the dynamics[32].

The state counting arguments given above rely on the assumption that the different combinations of $|N_{\mathrm{prod}}, L_{\mathrm{prod}}\rangle$ which satisfy equations (6) and (7) for a given pair of $|N_{K_2}, N_{Rb_2}\rangle$ are effectively degenerate in energy. In other words, the hyperfine structures of the K_2 and Rb_2 product molecules, along with any corresponding energy splittings that would break the degeneracy of the different $|N_{\mathrm{prod}}, L_{\mathrm{prod}}\rangle$ combinations associated with each $|N_{K_2}, N_{Rb_2}\rangle$ pair, have been ignored. For the purposes of this work, this assumption is justified as the energy splittings associated with the hyperfine structure of each product species are substantially smaller than the spectral resolution of the REMPI detection used in the experiment, which is approximately 45 MHz (ref. [32]).

Specifically, using the hyperfine Hamiltonian and calculated hyperfine coupling constants reported in ref. [48], along with the rotational and centrifugal constants given in Extended Data Table 2, we have calculated the spectral width of each rotational manifold. This is accomplished by diagonalizing the Hamiltonian in the presence of a 30 G magnetic field for each product species and including rotational states up to N_{K_2} =12 for the K_2 products and N_{Rb_2} =19 for the Rb_2 products. The spectral width here is defined as the energy difference between the highest energy hyperfine state and the lowest energy hyperfine state associated with a particular rotational quantum number. From the results of these calculations, we find that the spectral widths of the product rotational states that are relevant to this work, which arise from the hyperfine structure of each product species, are less than 1.11 MHz for Rb_2 and less than 0.27 MHz for K_2. Because this is substantially smaller than the experimental resolution of 45 MHz, the hyperfine structure of the products is not resolved and the different combinations of $|N_{\mathrm{prod}}, L_{\mathrm{prod}}\rangle$ associated with each pair of $|N_{K_2}, N_{Rb_2}\rangle$ can be considered degenerate.

We also note here that the spectral width associated with the hyperfine structure of the product molecules is smaller than the experimental uncertainty in the reaction exoergicity, $9.7711^{+0.0007}_{-0.0005}$ cm^{-1}, reported in the main text. In units of frequency, this uncertainty corresponds to an upper error bound of 20 MHz and a lower bound of 15 MHz, which are both larger than the hyperfine width of the product rotational states. We have therefore ignored the hyperfine structure of the products in determining the reaction exoergicity in the main text.

Resonance-enhanced multiphoton ionization of K_2 and Rb_2

The state-selective sampling of the reaction products is achieved via 1+1′ resonance-enhanced multiphoton ionization (REMPI), the schemes for which were first reported in our previous work[32]. In brief, to ionize K_2 (Rb_2) molecules that emerge from the reaction in a particular rovibronic state $X^1\Sigma_g^+(v=0, N_{K_2})$ ($X^1\Sigma_g^+(v=0, N_{Rb_2})$), we first resonantly drive a bound-to-bound transition to the excited state $B^1\Pi_u(v'=1, N_{K_2})$ ($B^1\Pi_u(v'=4, N_{Rb_2})$) using a continuous-wave diode laser with a wavelength around 648 nm (674) nm. The excited molecules are then ionized through a bound-to-continuum transition using a 532 nm pulsed YAG laser. The resonance frequency for each bound-to-bound transition is determined by scanning the frequency of the diode laser across the corresponding rovibronic resonance in the K_2 or Rb_2 product, and locating the frequency that yields the maximum ion counts. The initial search for these transitions is guided by frequencies that are calculated using molecular potentials from refs. [42,46,49,50]. All K_2 (Rb_2) bound-to-bound transitions targeted in this study share approximately the same transition dipole moment of 1.6 (1.5) ea_0, and are saturated at the diode laser intensity of 6.0 (5.5) mW mm^{-2} that we used. However, Doppler shifts due to finite product velocities introduce non-uniformities in the ionization efficiency of products in different quantum states, an effect that we account for using a numerical model later in Methods.

Experiment timing during ionization

Extended Data Fig. 1 illustrates the timing of the various lasers involved in the state-selective ionization of the reaction products. The reactant KRb molecules are created inside an optical-dipole trap (ODT) that has a peak optical intensity of 11.3 kW cm^{-2}. Shortly after creation, a 50% duty-cycle square-wave modulation at a 10 kHz repetition rate is applied to the ODT intensity to create alternating bright and dark phases. This allows reactions to occur without the interference of the ODT light for half the time, while also maintaining a time-averaged trapping potential for the KRb sample. In previous work, it was shown that the ODT light strongly photo-excites the $K_2Rb_2^*$ complex, which influences the reaction pathway[21]. During the dark phase of each ODT modulation period, 45 μs after the ODT turns off, we apply a REMPI pulse that consists of three wavelength components – 648 nm, 674 nm and 532 nm – to perform state-selective ionization of the reaction products.

During the bright phases of the ODT intensity modulation, reaction products are still being generated, albeit at a much lower rate compared to that during the dark phases. The quantum states of these products are unknown, but can potentially include the target state-pair of our REMPI, $|N_{K_2}, N_{Rb_2}\rangle$. Since our goal is to ionize products of the unperturbed KRb + KRb reaction during the dark phases, the ionization of products in the same target state-pair produced during the bright phases will confound our measurement. To avoid this, we apply, at the end each bright phase, a "cleanup" pulse that consists of a pulse of 648 and 674 nm lights at the same frequencies used in the REMPI pulse. This will photo-excite products in N_{K_2} and N_{Rb_2}, which, upon the ensuing spontaneous emission, will have negligible probabilities to decay back to the original states. As such, they will not be ionized by the following REMPI pulse. By monitoring the decay of the K_2^+ and Rb_2^+ signals over the course of the reaction, both in the presence and absence of the cleanup pulses, we found that these pulses do not noticeably perturb the reactants in the ODT.

Coincidence detection of product pairs

Coincidence imaging is a powerful tool for simultaneously probing multiple product molecules from individual reaction events. The driving force behind this technique is our three-dimensional detection system which is capable of measuring both the TOF and the transverse velocity of product ions. This information can be used to extract the three-dimensional momentum vectors of the initial product molecules, which enables the identification of coincident K_2 and Rb_2 product pairs based on the correlations of their momenta[38,51,52].

Following REMPI of the neutral product molecules, the resulting ions are accelerated towards a microchannel plate (MCP) detector (Roentdek DLD80) along the TOF axis, while simultaneously expanding ballistically at a rate determined by the initial velocities of their parent neutrals. The electrode plates providing the acceleration electric field operate in a velocity-map imaging configuration[53], such that the transverse momentum of each neutral product (p_x, p_y) is mapped onto its impact position on the detector (X, Y) according to the relations $p_{s,x} \propto \sqrt{2m_s}(X_s - X_s^0) = \sqrt{2m_s}\Delta X_s$ and $p_{s,y} \propto \sqrt{2m_s}(Y_s - Y_s^0) = \sqrt{2m_s}\Delta Y_s$. Here, s represents the product species (K_2 or Rb_2), m represents molecular mass, and $\{X_s^0, Y_s^0\}$ represents the impact position of zero-velocity products that is, in general, shifted from the detector centre due to the presence of Lorentz forces during the ion flight. The axial momentum of a product (p_z), on the other hand, is mapped into its TOF as a result of its location relative to the centre between the repeller and extractor plates[31], according to the relation $p_{s,z} \propto (\mathrm{TOF}_s - \mathrm{TOF}_s^0)/(\eta\Delta t/\mathrm{TOF}_s^0 - 1) = \Delta\mathrm{TOF}_s/(\eta\Delta t/\mathrm{TOF}_s^0 - 1)$. Here, TOF^0 represents the TOF for products with zero initial velocity, which is 69.27 μs and 102.13 μs for K_2 and Rb_2, respectively; Δt represents the time between the initial formation of the K_2 and Rb_2 product pair and its subsequent ionization (Extended Data Fig. 1), which can take any value in the range 0–45 μs; and η is a dimensionless parameter determined by the geometry of our electrodes, whose value is 136. Additional details of the ionization and detection setup are reported in ref. [30].

We identify coincidence ion pairs as those that satisfy the momentum conservation condition $\mathbf{p}_{K_2} + \mathbf{p}_{Rb_2} = 0$, or equivalently $p_{K_2,x} + p_{Rb_2,x} = 0$, $p_{K_2,y} + p_{Rb_2,y} = 0$, and $p_{K_2,z} + p_{Rb_2,z} = 0$. Given how a product molecule's momenta are related to its TOF and impact position, as well as the finite position and timing resolutions of our ion imaging system, the conservation of momentum translates into a set of screening criteria,

$$\left|\Delta X_{K_2} + \Delta X_{Rb_2}\sqrt{m_{Rb_2}/m_{K_2}}\right| \le n\sigma_X\sqrt{1 + m_{Rb_2}/m_{K_2}}, \tag{8}$$

$$\left|\Delta Y_{K_2} + \Delta Y_{Rb_2}\sqrt{m_{Rb_2}/m_{K_2}}\right| \le n\sigma_Y\sqrt{1 + m_{Rb_2}/m_{K_2}}, \tag{9}$$

$$\left|\Delta\mathrm{TOF}_{K_2} + \Delta\mathrm{TOF}_{Rb_2}\frac{\eta\Delta t/\mathrm{TOF}_{K_2}^0 - 1}{\eta\Delta t/\mathrm{TOF}_{Rb_2}^0 - 1}\right| \le n\sigma_T\sqrt{1 + \left(\frac{\eta\Delta t/\mathrm{TOF}_{K_2}^0 - 1}{\eta\Delta t/\mathrm{TOF}_{Rb_2}^0 - 1}\right)^2}. \tag{10}$$

Here, $\sigma_{X,Y,T}$ represent the 1σ resolution of our detection system along the X, Y and TOF axes, respectively, which are measured to be 0.23 mm, 0.23 mm and 11 ns. The multiplication factor n is empirically determined to be 3.

The efficacy of the above screening process is manifested in its ability to discriminate against uncorrelated ion counts, which we demonstrate in Fig. 2 using the product ion data for $|N_{K_2} = 6, N_{Rb_2} = 7\rangle$ as an example. Figure 2d shows the total number of detected K_2^+–Rb_2^+ pairs generated by two ionization pulses which are separated from one another by k pulses. There, one observes a prominent peak at $k = 0$, which corresponds to the number of simultaneously detected ion pairs, n_{sim}. The measured counts with $k \neq 0$, which correspond to uncorrelated ion pairs generated by separate pulses, form a uniform background with a mean value of n_{bkgd} and a standard deviation of δn_{bkgd}. Figure 2e shows the counts remaining after all ion pairs are subjected to screening based on equations (8) to (10). There, one observes a strong suppression of the background level, indicating that the uncorrelated pairs are effectively screened away. The height of the $k = 0$ peak is reduced, as accidental counts are screened away, while true coincidence counts

remain. Since the background level remains finite after screening, we use it as a proxy for the number of accidental counts that remain, and subtract it off to obtain the true coincidence counts, $n_{coin} = n_{sim} - n_{bkgd}$. The measured values of n_{sim}, n_{bkgd}, and δn_{bkgd} for all state-pairs are listed in Extended Data Table 4.

The uncertainty for the coincidence counts, δn_{coin}, has contributions from three sources – the shot noise associated with the simultaneous ion counts $\sqrt{n_{sim}}$, the fluctuation of the background level δn_{bkgd}, and the fluctuation in experimental conditions (αn_{coin}, see the following section). Since these errors are uncorrelated, they are summed in quadrature to yield the overall uncertainty, $\delta n_{coin} = \sqrt{n_{sim} + (\delta n_{bkgd})^2 + (\alpha \times n_{coin})^2}$. For state-pairs with sufficient statistics ($n_{sim} \geq 5$), which makes up the vast majority of the measured state-pairs, the contribution of δn_{bkgd} to the overall uncertainty is very small (<5%). The values for δn_{coin} are reflected by the error bars in Fig. 3b–h, whose sizes are $\pm\delta n_{coin}$. This uncertainty is propagated into that of the normalized coincidence counts as well as the measured scattering probabilities that constitute the product state distribution P_{sc}^{meas}.

We note that while methods for obtaining coincident quantum state information for a pair of products already exist[54,55], their resolution is insufficient for resolving the small spacing between rotational levels of heavy molecules such as K_2 and Rb_2. Hence the current scheme represents a new approach to complete product state detection that is generally applicable to reactions involving polyatomic species.

Normalization of coincidence counts

The screening process described in the previous section allows us to extract the number of coincidence ion pair counts, $n_{coin}(N_{K_2}, N_{Rb_2})$, from the dataset associated with each given state-pair. In order for $n_{coin}(N_{K_2}, N_{Rb_2})$ to proportionally reflect the scattering probability into $|N_{K_2}, N_{Rb_2}\rangle$, however, it must undergo normalizations against experimental biases that differ from one dataset to another. Sources for these biases include the number of experimental cycles associated with each dataset, fluctuations in experimental conditions between datasets, and the product-velocity-dependent efficiency of our REMPI sampling. In this section, we describe the procedures used to account for these biases.

Normalization against product-velocity-dependent ionization sampling efficiency. In our experiment, products generated by the reaction are sampled in a state-dependent fashion using REMPI. The efficiency of this sampling depends on the product velocities due to two mechanisms: (1) high-velocity products have a higher chance of escaping the volume covered by the REMPI beams before the REMPI lasers are pulsed on; and (2) products with velocity components along or against the direction of REMPI beam propagation will experience Doppler shifts to the bound-to-bound transition frequency, which affects the probability for the product to be promoted to the excited state. We can respectively quantify the degree to which these two mechanisms affect the sampling of correlated product pairs using a geometric factor, $F_{geometry}(T)$, and a Doppler factor, $F_{Doppler}(T)$. Here, T represents the translational energy of products in a given state-pair, and is related to the product velocities as $v_{K_2}(T) = \sqrt{2Tm_{Rb_2}/(m_{Rb_2} + m_{K_2})/m_{K_2}}$ and $v_{Rb_2}(T) = \sqrt{2Tm_{K_2}/(m_{Rb_2} + m_{K_2})/m_{Rb_2}}$. In this section, we develop models for these factors.

Physically, the geometric factor represents the fraction of product pairs that are generated during the dark phase of the ODT modulation (Extended Data Fig. 1), and remain inside the volume exposed to the REMPI beam when it is pulsed on. Over the region of interest, our REMPI beam can be approximated as a 1mm-diameter cylinder with a uniform intensity (for each frequency component). Since a K_2 product molecule will always travel faster compared to its Rb_2 coproduct, $F_{geometry}$ is determined solely by the fraction of K_2 molecules that remain within the beams given their velocity. To model this factor, we developed a numerical simulation that generates and samples reaction products according to the beam geometry and timing diagram shown in the insets of Extended Data Fig. 2. The simulation takes the velocity of the products and other parameters from the experiment (that is, repetition rate f and details of the timing) as inputs, and reports the fraction of products exposed to the REMPI beam over many detection periods. In brief, each period of the REMPI detection begins with the turn off of the ODT confining the KRb molecules, at which point products begin to emerge from reactions with velocity v and propagate outward; after a time t_{del}, the REMPI beams are pulsed on, and the number of products under its exposure is accumulated; this period is repeated several hundred times to collect statistics. In the end, the number of exposed products is divided by the total number of products generated to obtain the exposed fraction $F_{geometry}(v)$.

Extended Data Fig. 2 shows $F_{geometry}(v)$ over the range of expected velocities for K_2 ($v = 0–44$ m s^{-1}). It is calculated according to the timing scheme used in the experiment (see Extended Data Fig. 1), that is, $f = 10$ kHz, $t_{del} = 45$ μs, and a 50% duty-cycle for the ODT modulation. Products with $v > 11.1$ m s^{-1} are fully contained within the cylindrical volume before ionization, and therefore have $F_{geometry}(v) = 1$; those with $v > 11.1$ m s^{-1}, on the other hand, experience a decay in $F_{geometry}(v)$ that approximately scales as $1/v$. Using the simulation result, we calculated, for all allowed state-pairs, the geometric factor relevant for the normalization of coincidence counts $F_{geometry}(T)$.

To characterize the Doppler effect on the product sampling, we use a method based on density matrix equations to analyse the dynamics of the REMPI process[56]. The 1 + 1′ REMPI technique used here consists of an initial single-photon bound-to-bound transition from the electronic and vibrational ground state $X^1\Sigma_g^+(v = 0, N)$ to an electronically excited intermediate-state $B^1\Pi_u(v', N')$, followed by a single-photon bound-to-continuum transition that ionizes the molecules. We drive the bound-to-bound transition using a frequency-tunable laser operating around 648 nm for the detection of K_2 and 674 nm for Rb_2. The bound-to-continum transition is excited by a 532 nm pulsed laser for both product species. For the convenience of discussion, the ground state is denoted by $|0\rangle$ and the intermediate-state is denoted by $|1\rangle$. The differential equations for the components of the density matrix which describe the dynamics of the REMPI process can be written as

$$\frac{d}{dt}\rho_{00}(t) = -\frac{i}{2}(\Omega_{01}\rho_{10} - \text{c.c.}), \tag{11}$$

$$\frac{d}{dt}\rho_{11}(t) = -(\Gamma_1 + \Gamma_{ion})\rho_{11} + \frac{i}{2}(\Omega_{01}\rho_{10} - \text{c.c.}), \tag{12}$$

$$\frac{d}{dt}\rho_{10}(t) = -\frac{1}{2}(\Gamma_1 + \Gamma_{ion})\rho_{10} + i\Delta_1\rho_{10} + \frac{i}{2}\Omega_{10}(\rho_{11} - \rho_{00}), \tag{13}$$

where c.c. stands for complex conjugate, Ω_{01} is the Rabi frequency of the bound-to-bound transition, $\Delta_1 = \omega - \omega_0$ is the detuning, Γ_1 is the spontaneous decay rate of $|1\rangle$, and Γ_{ion} is the ionization rate of the bound-to-continuum transition. Here $\hbar\omega_0$ represents the resonant transition energy and $\hbar\omega$ is the photon energy. To consider realistic intensity profiles of the REMPI laser pulses over time, the corresponding time-dependent rates $\Omega_{01}(t)$ and $\Gamma_{ion}(t)$ are used in the numerical calculation (Extended Data Fig. 3a). The ionization probability can be extracted via $P_{ion} = \int P_{loss}(t)\frac{\Gamma_{ion}(t)}{\Gamma_1 + \Gamma_{ion}(t)}dt$, with $P_{loss}(t) = 1 - \rho_{00}(t) - \rho_{11}(t)$. To take into account the Doppler effect, ω_0 is replaced by $\omega_0(1 + v_z/c)$ and the ionization probability thus becomes v_z-dependent, where v_z is the projection of the product's velocity onto the propagation direction of the REMPI beams and c is the speed of light. The formula for $P_{ion}(v_z)$, after substituting the corresponding values of the parameters Γ_1, Γ_{ion},

Ω_{01} and Δ_1, applies to both K_2 and Rb_2 products. We use $P_{ion}^{K_2}(v_z)$ and $P_{ion}^{Rb_2}(v_z)$ to denote the ionization probabilities of the two species, respectively.

For the coincidence detection scheme used in this work, the probability of simultaneously ionizing a correlated product pair is $P_{ion}^{coin}(v_z) = P_{ion}^{K_2}(v_z)P_{ion}^{Rb_2}(-m_{K_2}v_z/m_{Rb_2})$, where v_z here represents the velocity projection of K_2 on the REMPI beam direction and $-m_{K_2}v_z/m_{Rb_2}$ is that of Rb_2 obtained based on the momentum conservation. By averaging over all possible directions of the product's velocity, the factor that characterizes the Doppler effect on the measurement efficiency of a correlated product pair is derived to be $F_{Doppler}(v) = \frac{1}{2v}\int_{-v}^{v} dv_z P_{ion}^{coin}(v_z)/P_{ion}^{coin}(v_z = 0)$, where v is the magnitude of the velocity of K_2 and is determined by the quantum states of products and the reaction exoergicity. The factor $F_{Doppler}(v)$ is calculated by solving the differential equations (equations (11)–13) as a function of v, as shown in Extended Data Fig. 3b. In the calculation, we used $\Gamma_1/(2\pi) = 14$ MHz, $\Delta_1 = 0$, a peak value of $\Omega_{01}(t)$ at $2\pi \times 58$ MHz, which is estimated using the calculated transition dipole moment and the measured laser intensity, and a peak value of $\Gamma_{ion}(t)$ at $2\pi \times (10 \pm 4)$ MHz estimated based on the measured ionization efficiency.

Normalization against fluctuations in experimental conditions. In a given experiment where we probe a state-pair $|N_{K_2}, N_{Rb_2}\rangle$, the number of detected coincidence counts, n_{coin}, is proportional to the product of the state-dependent ionization probabilities, $P_{ion}(N_{K_2})P_{ion}(N_{Rb_2})$. Across different experiments, drifts in the power, detuning, and relative timing of the REMPI lasers introduce fluctuations to $P_{ion}(N_{K_2})$ and $P_{ion}(N_{Rb_2})$, resulting in a biased sampling of coincidence counts. To correct against such an effect, we note that, in the same experiment, the total number of K_2^+ and Rb_2^+ ion counts, $n_{K_2^+}$ and $n_{Rb_2^+}$, are proportional to $P_{ion}(N_{K_2})$ and $P_{ion}(N_{Rb_2})$ respectively, and thus experience the same fluctuations. This allows us to construct a normalization factor as

$$S(N_{K_2}, N_{Rb_2}) = \frac{n_{K_2^+}(N_{K_2}, N_{Rb_2})n_{N_{Rb_2}^+}(N_{K_2}, N_{Rb_2})}{\langle n_{K_2^+}(N'_{K_2} = N_{K_2}, N'_{Rb_2})\rangle\langle n_{Rb_2^+}(N'_{K_2}, N'_{Rb_2} = N_{Rb_2})\rangle}, \quad (14)$$

where $\langle n_{K_2^+}(N'_{K_2} = N_{K_2}, N'_{Rb_2})\rangle$ is the average value of the number of K_2^+ ions from all experiments that share a common value for N_{K_2}, and $\langle n_{Rb_2^+}(N'_{K_2}, N'_{Rb_2} = N_{Rb_2})\rangle$ is the average value of the number of Rb_2^+ ions from all experiments that share a common value for N_{Rb_2}. We assess the effectiveness of this method of normalization by examining the relative differences in the coincidence counts obtained from two separate experiments on the same state-pairs, before and after applying the S factor. From 11 different state-pairs where repeated data are available, we find that the average fluctuation in n_{coin} decreases from $\alpha = 0.11$ to $\alpha = 0.054$ after normalization. Since this method of normalization is somewhat ad hoc, we retain the conservative value of $\alpha = 0.11$ for purposes of estimating experimental errors and hypothesis testing despite applying this normalization to all measured data.

Using the factors $F_{geometry}$, $F_{Doppler}$ and S from the above derivations, as well as the number of cycles associated with each experiment, C_{exp}, we arrive at an overall normalization factor

$$G(N_{K_2}, N_{Rb_2}) = \frac{C_{exp}(N_{K_2}, N_{Rb_2})F_{geometry}(N_{K_2}, N_{Rb_2})F_{Doppler}(N_{K_2}, N_{Rb_2})S(N_{K_2}, N_{Rb_2})}{\sum_{\{N'_{K_2}, N'_{Rb_2}\}} C_{exp}(N'_{K_2}, N'_{Rb_2})F_{geometry}(N'_{K_2}, N'_{Rb_2})F_{Doppler}(N'_{K_2}, N'_{Rb_2})S(N'_{K_2}, N'_{Rb_2})}. \quad (15)$$

Here, the sum in the denominator is carried out over the datasets for all state-pairs that we probed in this study, including 57 allowed pairs (S) and two forbidden ones ($|10, 13\rangle$ and $|10, 15\rangle$). Applying this overall factor to all detected coincidence counts, we obtain the normalized coincidence counts as $\mathcal{N}_{coin}(N_{K_2}, N_{Rb_2}) = n_{coin}(N_{K_2}, N_{Rb_2})/G(N_{K_2}, N_{Rb_2})$. We note that, owing to the normalizations, $\mathcal{N}_{coin}$ can take on non-integer values. The scattering probabilities (Fig. 3) then derive from the normalized coincidence counts according to $P_{sc}^{meas}(N_{K_2}, N_{Rb_2}) = \mathcal{N}_{N_{K_2}, N_{Rb_2}}/\sum_{\mathcal{S}} \mathcal{N}_{N_{K_2}, N_{Rb_2}}$.

Likelihood ratio test for the statistical model

The degree to which the measured product state distribution (P_{sc}^{meas}) agrees with the state-counting model (P_{sc}^{0}) is quantified using the likelihood ratio test[39]. Formally, we test the null hypothesis $H_0: \theta \in \boldsymbol{\Theta}_0$, where $\theta = \{\mu_t(N_{K_2}, N_{Rb_2})\}_{\mathcal{S}}$ represents the set of mean coincidence counts given the true product state distribution, $\boldsymbol{\Theta}_0 = \{\mu_0(N_{K_2}, N_{Rb_2})\}_{\mathcal{S}}$ represents the set of mean coincidence counts given the statistical model, and S is the entire set of allowed state-pairs. The values for μ_0 depend both on the model and the experimental biases in our sampling of coincidence counts, and is expressed as

$$\mu_0(N_{K_2}, N_{Rb_2}) = \frac{P_{sc}^0(N_{K_2}, N_{Rb_2})G(N_{K_2}, N_{Rb_2})}{\sum_{\mathcal{S}} P_{sc}^0(N_{K_2}, N_{Rb_2})G(N_{K_2}, N_{Rb_2})} n_{coin}^{tot}, \quad (16)$$

where G represents the overall normalization factor, and $n_{coin}^{tot} = \sum_{\mathcal{S}} n_{coin}(N_{K_2}, N_{Rb_2})$ represents the sum of the set of all measured coincidence counts $\{n_{coin}(N_{K_2}, N_{Rb_2})\}_{\mathcal{S}}$.

The likelihood for H_0 is given by

$$\mathcal{L}_{\mathcal{S}}(\hat{\theta}_0) = \prod_{\mathcal{S}} P_c[n_{coin}(N_{K_2}, N_{Rb_2}), \mu_0(N_{K_2}, N_{Rb_2})]. \quad (17)$$

Here, $\mathcal{L}_{\mathcal{S}}$ represents the likelihood function, $\hat{\theta}_0$ is the maximum likelihood estimate (MLE) when θ is restricted to lie in $\boldsymbol{\Theta}_0$, and $P_c(n_{coin}, \mu_0)$ is the probability of observing a particular count n_{coin} given a mean count of μ_0. Since the accumulation of coincidence counts for each state-pair is a constant-rate process, we model P_c as a Poisson distribution, but with an uncertainty in its mean introduced by experimental fluctuations captured by a Gaussian function. It is expressed as

$$P_c(x, \mu, \alpha) = [f(x) * g(\alpha)](\mu) = \int_0^{\infty}\left(\frac{e^{-m}m^x}{x!}\right)\left(\frac{1}{\alpha\mu\sqrt{2\pi}}e^{-\frac{1}{2}\left(\frac{m-\mu}{\alpha\mu}\right)^2}\right)dm. \quad (18)$$

Here, $f(x,m) = e^{-m}m^x/x!$ represents a Poisson distribution with mean m, and $g(m, \mu, \alpha) = (\alpha\mu\sqrt{2\pi})^{-1}\exp[-(m-\mu)^2/(\alpha\mu)^2/2]$ represents a normal distribution with mean μ and standard deviation α. Note that α characterizes the relative fluctuation of the mean, and has an empirically-determined value of $\alpha_0 = 0.11$ for our measurements.

By maximizing $\mathcal{L}_{\mathcal{S}}$ over $\boldsymbol{\Theta}_0$, we obtain the maximum likelihood for the observed outcome, $\mathcal{L}_{\mathcal{S}}(\hat{\theta})$. Here, $\hat{\theta}$ represents the MLE of the parameters. Given $\mathcal{L}_{\mathcal{S}}(\hat{\theta}_0)$ and $\mathcal{L}_{\mathcal{S}}(\hat{\theta})$, we can calculate the likelihood ratio statistic as

$$\lambda_{\mathcal{S}} = 2\log\left(\frac{\mathcal{L}_{\mathcal{S}}(\hat{\theta})}{\mathcal{L}_{\mathcal{S}}(\hat{\theta}_0)}\right). \quad (19)$$

Within the framework of the likelihood ratio test, the P-value for H_0 is

$$P_{\mathcal{S}} = \mathbb{P}(\chi_k^2 > \lambda_{\mathcal{S}}). \quad (20)$$

Here, $\mathbb{P}$ represents probability, χ_k^2 is the chi-square distribution with k degrees of freedom, and k is the length of $\mathcal{S}$, which is determined to be 57 in our study. We use $P_{\mathcal{S}} < 0.001$ as a threshold for rejecting H_0.

Using the values for $\{n_{coin}(N_{K_2}, N_{Rb_2})\}_{\mathcal{S}}$ and $\{\mu_0(N_{K_2}, N_{Rb_2})\}_{\mathcal{S}}$ obtained from this work, we find $\lambda_{\mathcal{S}} = 276$ and $p_{\mathcal{S}} \approx 10^{-30}$ for $\alpha_0 = 0.11$. This means that H_0 should be rejected, and the outcome of our measurements is inconsistent with the state-counting model based on statistical theory.

On the other hand, we can test whether the model describes a subset of our measurements. To this end, we successively remove, from the above analysis, the state-pair that displays the largest deviation from the model prediction, and recalculate the P-value for H_0. To quantify

the degree of deviation for each state-pair, we calculate its state-specific likelihood ratio statistic

$$\lambda_{N_{K_2},N_{Rb_2}} = 2\log\left(\frac{\max_{\mu_0\in[0,\infty]}\{P_c\,[n_{coin}(N_{K_2},N_{Rb_2}),\mu_0(N_{K_2},N_{Rb_2})]\}}{P_c\,[n_{coin}(N_{K_2},N_{Rb_2}),\mu_0(N_{K_2},N_{Rb_2})]}\right), \quad (21)$$

as well as the associated P-value, $P_{N_{K_2},N_{Rb_2}} = \mathbb{P}(\chi_1^2 > \lambda_{N_{K_2},N_{Rb_2}})$. The results are displayed in Extended Data Table 4. The state-pair that deviates the most from the state-counting model is $|12, 7\rangle$ ($P = 10^{-18}$), which we have identified to be a near-threshold state-pair for which the long-range centrifugal barriers strongly suppress product formation. Other state-pairs that strongly deviate include the ones with low translational energies, for example, $|12, 5\rangle$ ($P = 10^{-6}$) and $|8, 15\rangle$ ($P = 10^{-11}$).

Let $\mathcal{S}^{(j)} = \mathcal{S} - \{\mathcal{S}_1, \ldots, \mathcal{S}_j\}$ denote the reduced set for which the first j members of $\mathcal{S}$ with the smallest state-specific P-values are removed. Using equations (16)–(20), we calculate the P-values for the reduced sets, $P_{\mathcal{S}^{(j)}}$, for $j = 0, 1, \ldots, 57$. The results are shown in Fig. 3i. Here, one observes that the P-value for H_0 increases monotonically as we successively remove the largest outliers, and increases above the 0.001 threshold for rejecting H_0 after 7 state-pairs are removed. In other words, for a subset that contains the majority (50) of the allowed state-pairs, we find the measured outcome to be consistent with the state-counting statistical model.

Distribution of product translational energy

In a 2012 review article[28], Nesbitt speculated that energy deposition into product translation should be dynamically disfavoured for ultracold complex-forming reactions such as KRb + KRb. The basis for this speculation is the observed propensity for complexes bound by van dar Waals forces to strongly favour the formation of low translational energy products upon their dissociation. Here, we examine whether such a propensity exists in our result by displaying the measured and predicted scattering probabilities for all allowed product state-pairs as functions of their translational energy, and searching for any systematic trends in how they deviate from each other (Extended Data Fig. 4). To this end, we construct 'blurred' distributions by applying a Gaussian broadening of 0.25 cm^{-1} 1σ width to the measured and predicted amplitudes of each state-pair. Comparing the two blurred distributions, we do not observe any strong monotonic trends in their difference.

Product escape probabilities

In this section, we calculate the probability for products to escape from the complex and into each allowed state-pair. For this purpose, we consider the microscopically reverse process of product capture into the complex, and the associated capture probability $\mathcal{C}(N_{K_2}, N_{Rb_2})$. The details of the implementation for diatom-diatom systems have been published in ref. [43]. In brief, the time-independent Schrödinger equation is solved in diatom–diatom Jacobi coordinates (R, r_1, r_2, θ_1, θ_2, ϕ) using the log-derivative method[57,58] with the Wentzel-Kramers-Brillouin (WKB) approximation[59] to damp the wavefunction within the capture radius. The interaction potential is determined using a similar method as in ref. [43]. In the calculations, only the p-wave ($L_{reac} = 1$) and $\varepsilon = -1$ were considered, given the fermionic nature of the KRb reactants. 3/3/15/15/20 points were used for the $r_1/r_2/\theta_1/\theta_2/\phi$ quadratures. The log-derivative propagation steps are chosen as $\Delta R = 0.05a_0$ for $R \in [35.0, 80.0]a_0$, $\Delta R = 0.5a_0$ for $R \in [80.0, 200.0]a_0$, and $\Delta R = 1.00a_0$ for $R \in [200.0, 800.0]a_0$, respectively. The number of rotational bases is chosen to be $N_{K_2}^{max} = 20$ and $N_{Rb_2}^{max} = 30$. The effective potentials for the calculation are defined in the manner of adiabatic channel potential energy, as

$$V_\xi^{eff}(R) = W_{\xi,\xi}(R) + \frac{L_{prod}(L_{prod}+1)}{2\mu_{K_2,Rb_2}R^2}. \quad (22)$$

Here, $\xi = \{N_{K_2}, N_{Rb_2}, N_{prod}, L_{prod}\}$ is the set of product quantum numbers, $W_{\xi,\xi}$ is the diagonal element of interaction potential matrix in the space-fixed frame, which can be calculated by an orthogonal transformation from the body-fixed counterpart. The results show that all allowed state-pairs besides $|12, 7\rangle$ have effectively unit probabilities ($\mathcal{C} > 0.999$) to escape the complex, indicating that product formation in these state-pairs is not hindered by any barriers or bottlenecks.

Data availability

The data that support the findings of this study are available from the corresponding author upon reasonable request.

Code availability

The computer codes used for theoretical calculations in this study are available from H.G. (hguo@unm.edu) upon reasonable request.

46. Falke, S., Sherstov, I., Tiemann, E. & Lisdat, C. The $A^1\Sigma_u^+$ state of K_2 up to the dissociation limit. *J. Chem. Phys.* **125**, 224303 (2006).
47. Amiot, C. Laser-induced fluorescence of Rb_2: the (1) $^1\Sigma_g^+(X)$, (2) $^1\Sigma_g^+$, (1) $^1\Pi_u(B)$, (1) $^1\Pi_g$, and (2) $^1\Pi_g(C)$ electronic states. *J. Chem. Phys.* **93**, 8591–8604 (1990).
48. Aldegunde, J. & Hutson, J. M. Hyperfine energy levels of alkali-metal dimers: ground-state homonuclear molecules in magnetic fields. *Phys. Rev. A* **79**, 013401 (2009).
49. Caldwell, C., Engelke, F. & Hage, H. High resolution spectroscopy in supersonic nozzle beams: the Rb_2 $B^1\Pi_u - X_1\Sigma_g^+$ band system. *Chem. Phys.* **54**, 21–31 (1980).
50. Amiot, C. & Vergès, J. Optical-optical double resonance and Fourier transform spectroscopy: the Rb_2 $B_1\Pi_u$ electronic state up to the quasibound energy levels. *Chem. Phys. Lett.* **274**, 91–98 (1997).
51. Ullrich, J. et al. Recoil-ion and electron momentum spectroscopy: reaction-microscopes. *Rep. Prog. Phys.* **66**, 1463 (2003).
52. Vredenborg, A., Roeterdink, W. G. & Janssen, M. H. A photoelectron-photoion coincidence imaging apparatus for femtosecond time-resolved molecular dynamics with electron time-of-flight resolution of σ = 18 ps and energy resolution $\Delta E/E$ = 3.5%. *Rev. Sci. Instrum.* **79**, 063108 (2008).
53. Eppink, A. T. & Parker, D. H. Velocity map imaging of ions and electrons using electrostatic lenses: application in photoelectron and photofragment ion imaging of molecular oxygen. *Rev. Sci. Instrum.* **68**, 3477–3484 (1997).
54. Gericke, K.-H. Correlations between quantum state populations of coincident product pairs. *Phys. Rev. Lett.* **60**, 561 (1988).
55. Lin, J. J., Zhou, J., Shiu, W. & Liu, K. State-specific correlation of coincident product pairs in the F + CD_4 reaction. *Science* **300**, 966–969 (2003).
56. Dixit, S., Levin, D. & McKoy, B. Resonant enhanced multiphoton ionization studies in atomic oxygen. *Phys. Rev. A* **37**, 4220 (1988).
57. Johnson, B. An improved log derivative method for inelastic scattering. *J. Comput. Phys.* **13**, 445–449 (1973).
58. Manolopoulos, D. An improved log derivative method for inelastic scattering. *J. Chem. Phys.* **85**, 6425–6429 (1986).
59. Johnson, B. A generalized JWKB approximation for multichannel scattering. *Chem. Phys.* **2**, 381–399 (1973).

Acknowledgements We thank L. Zhu for experimental assistance; T. Rosenband, G. Quéméner, W. Cairncross, E. Heller and M. Soley for discussions; T. Karman for providing the code for state-counting; J. Huang for ab initio calculations; and L. Liu for a critical reading of the manuscript. This work is supported by the DOE Young Investigator Program (DE-SC0019020) and the David and Lucile Packard Foundation. M.A.N. is supported by the Arnold O. Beckman Postdoctoral Fellowship in Chemical Instrumentation. D.Y. and D.X. acknowledge support from the National Natural Science Foundation of China (grant numbers 21733006). H.G. thanks the Army Research Office (W911NF-19-1-0283) for funding.

Author contributions The experimental work and data analysis were carried out by Y.L., M.-G.H., M.A.N. and K.-K.N. Theoretical calculations were performed by D.Y., D.X. and H.G. All authors contributed to interpreting the results and writing the manuscript.

Competing interests The authors declare no competing interests.

Additional information

Correspondence and requests for materials should be addressed to Y.L. or K.-K.N.

Peer review information *Nature* thanks Simon Cornish, Nandini Mukherjee and the other, anonymous, reviewer(s) for their contribution to the peer review of this work.

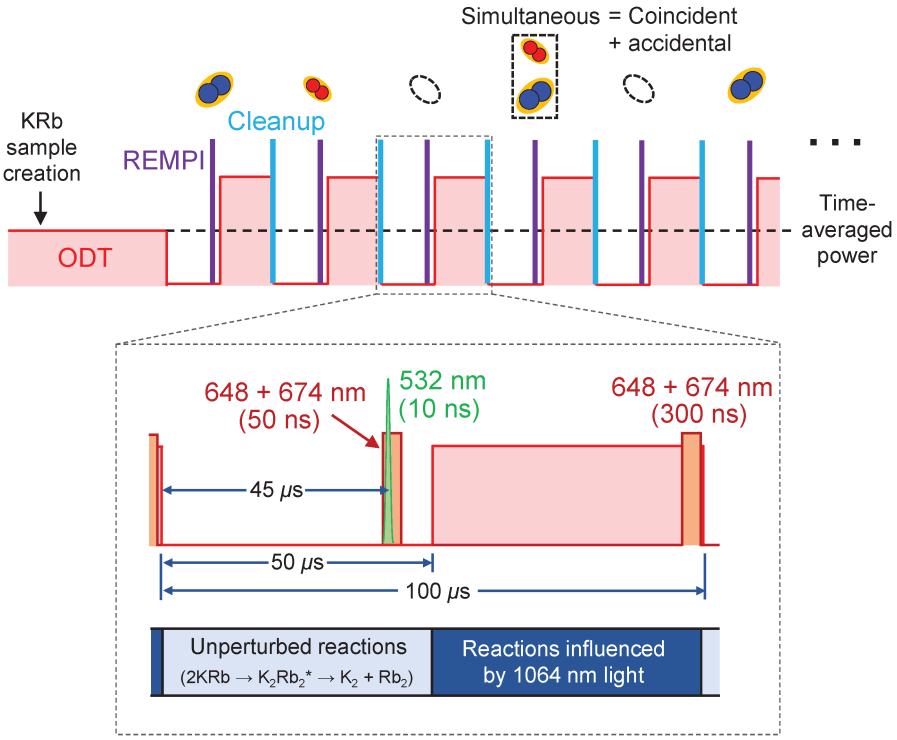

Extended Data Fig. 1 | Timing diagram for product ionization. The relative timing between the ODT, REMPI, and cleanup pulses during the state-selective ionization of reaction products. The inset shows a close-up view of a single modulation period. Unperturbed reactions occur during the dark phase of the period, while reactions influenced by the (1,064 nm) ODT light occur during the bright phase. The numbers in parentheses indicate pulse durations.

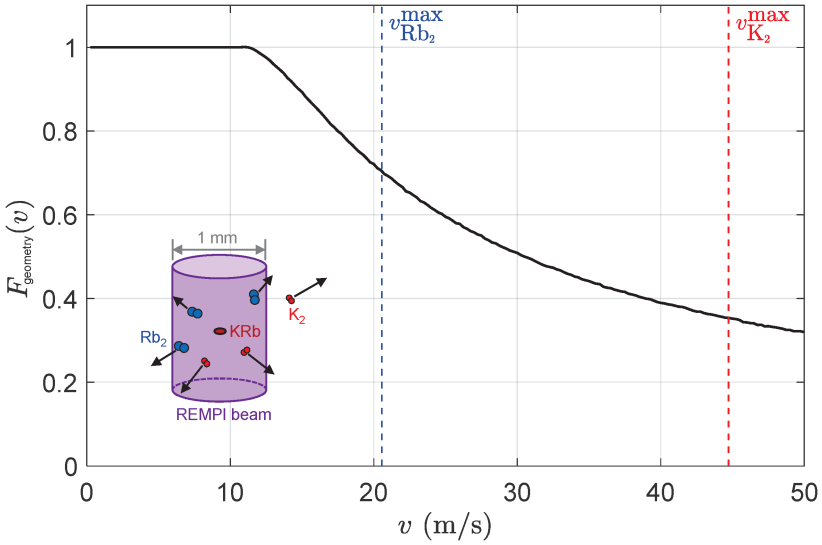

Extended Data Fig. 2 | Modelling the geometric factor for product sampling. The plot shows the fraction of product pairs that remain within the REMPI beam volume at the time of ionization as a function of the velocity of the K_2 product within the pair. Blue and red dashed lines indicate the maximum velocities of the K_2 and Rb_2 products, respectively. The inset shows the ionization geometry.

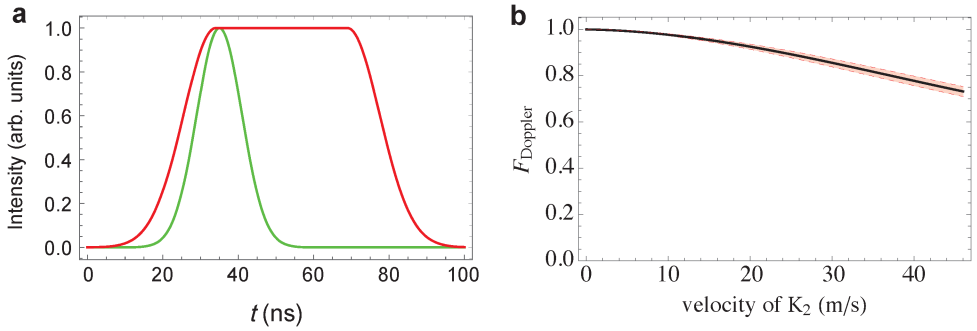

Extended Data Fig. 3 | Modelling the Doppler factor for product sampling. **a**, Normalized optical intensity profiles of the REMPI laser pulses. The red trace corresponds to the 648 nm or 674 nm lights, and is proportional to Ω_{01}. The green trace corresponds to the 532 nm light, and is proportional to Γ_{ion}. **b**, The Doppler factor $F_{Doppler}(v)$ versus the velocity of the K_2 product. The lower and upper bounds correspond to $\Gamma_{ion}/(2\pi)$ at peak values of 6 MHz and 14 MHz, respectively.

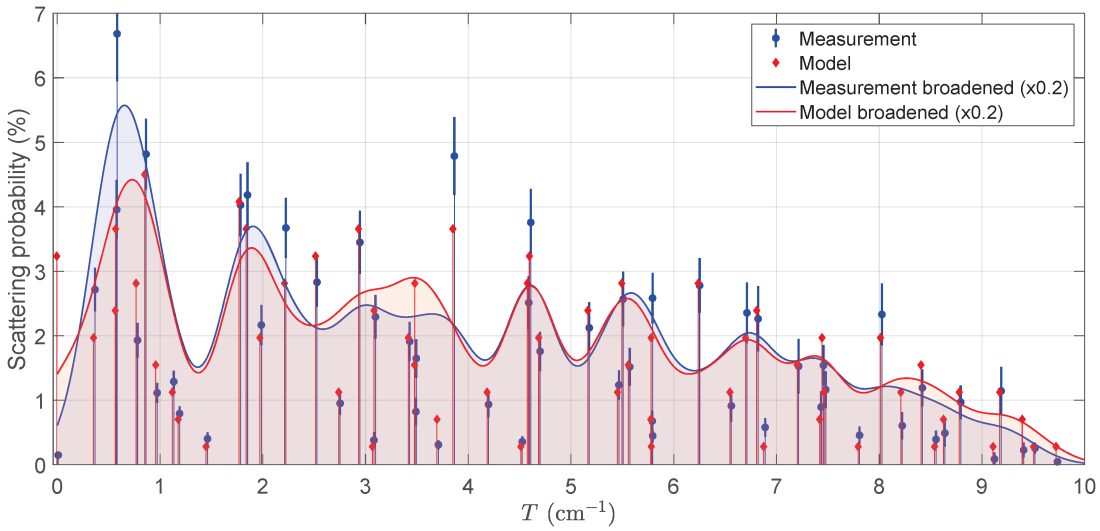

Extended Data Fig. 4 | Distribution of product translational energy. The measured (blue circle) and predicted (red diamond) scattering probabilities for all allowed state-pairs are plotted versus their translational energies (T). The two sets of points are offset horizontally by 0.014 cm^{-1} for clarity. To aid in the identification of systematic deviations, we multiply each scattering probability by a normalized Gaussian function with a 1σ width of 0.25 cm^{-1}, and sum them up to construct broadened distributions as shown by the blue and red curves. These curves are scaled by a factor of 0.2 for convenience.

Extended Data Table 1 | Molecular dissociation energies of $^{40}K^{87}Rb$, $^{40}K_2$ and $^{87}Rb_2$

Species	D_e (cm^{-1})	ω_0 (cm^{-1})	D_0 (cm^{-1})	Reference
$^{40}K^{87}Rb$			-4180.442	29
$^{40}K_2$	-4450.904(4)	91.032(1)	-4405.389(4)	46
$^{87}Rb_2$	-3993.53(6)	57.121(1)	-3964.97(6)	42

D_e: well depth; ω_0: vibrational constant; D_0: dissociation energy.

Extended Data Table 2 | Rotational and centrifugal distortion constants for $^{40}K_2$ and $^{87}Rb_2$

Quantity	Symbol	Value (cm^{-1})	Reference
$^{40}K_2$ rotational constant	B_{K_2}	$5.478155(84)\times10^{-2}$	41
$^{40}K_2$ centrifugal constant	D_{K_2}	$7.8641(68)\times10^{-8}$	41
$^{87}Rb_2$ rotational constant	B_{Rb_2}	$2.188943(61)\times10^{-2}$	42
$^{87}Rb_2$ centrifugal constant	D_{Rb_2}	$1.29507(56)\times10^{-8}$	42

Values are scaled by mass from the measured values for $^{39}K_2$ and $^{85}Rb_2$.

Extended Data Table 3 | The internal energy (*U*) and degeneracy ($\mathcal{D}$) for all measured product state-pairs

N_{K_2}	N_{Rb_2}	$U(cm^{-1})$	$\mathcal{D}$	N_{K_2}	N_{Rb_2}	$U(cm^{-1})$	$\mathcal{D}$	N_{K_2}	N_{Rb_2}	$U(cm^{-1})$	$\mathcal{D}$
0	1	0.043779(1)	2	4	1	1.13938(1)	5	8	3	4.20654(4)	11
0	3	0.262671(7)	2	4	3	1.35827(1)	11	8	5	4.60054(5)	17
0	5	0.65667(2)	2	4	5	1.75227(2)	14	8	7	5.16963(6)	23
0	7	1.22577(3)	2	4	7	2.32137(4)	14	8	9	5.91381(7)	26
0	9	1.96994(5)	2	4	9	3.06554(6)	14	8	11	6.83304(9)	26
0	11	2.88918(8)	2	4	11	3.98478(8)	14	8	13	7.9273(1)	26
0	13	3.9834(1)	2	4	13	5.0791(1)	14	8	15	9.1966(2)	26
0	15	5.2527(1)	2	4	15	6.3483(1)	14	10	1	6.06880(7)	5
0	17	6.6970(2)	2	4	17	7.7926(2)	14	10	3	6.28769(7)	11
0	19	8.3161(2)	2	4	19	9.4117(2)	14	10	5	6.68169(7)	17
2	1	0.372465(4)	5	6	1	2.34447(3)	5	10	7	7.25079(8)	23
2	3	0.591358(8)	8	6	3	2.56336(3)	11	10	9	7.99496(9)	29
2	5	0.98536(2)	8	6	5	2.95736(3)	17	10	11	8.9142(1)	32
2	7	1.55445(3)	8	6	7	3.52645(4)	20	10	13†	10.0085(1)	32
2	9	2.29863(5)	8	6	9	4.27063(6)	20	10	15†	11.2777(2)	32
2	11	3.21787(8)	8	6	11	5.18987(8)	20	12	1	8.5878(1)	5
2	13	4.3121(1)	8	6	13	6.2841(1)	20	12	3	8.8067(1)	11
2	15	5.5814(1)	8	6	15	7.5534(1)	20	12	5	9.2007(1)	17
2	17	7.0256(2)	8	6	17	8.9976(2)	20	12	7	9.7678(1)	23
2	19	8.6448(2)	8	8	1	3.98764(4)	5				

The uncertainty (number in parentheses) associated with each internal energy value is derived from the uncertainties of the molecular constants reported in Extended Data Table 2 through standard error propagation. Energetically forbidden state pairs are labelled with †.

Extended Data Table 4 | Various measured quantities that are used towards calculating the scattering probability into each product state-pair

N_{K_2}	N_{Rb_2}	C_{exp}	n_{sim}	n_{bkgd}	δn_{bkgd}	$\log(p)$	N_{K_2}	N_{Rb_2}	C_{exp}	n_{sim}	n_{bkgd}	δn_{bkgd}	$\log(p)$
0	1	1947	2	0.2	0.4	-2.8	6	1	1629	17	0.6	0.7	-0.3
0	3	1603	11	0.6	0.7	-0.2	6	3	820	18	1	1	0.0
0	5	1402	2	0.6	0.7	-1.3	6	5	859	34	2.8	1.7	-0.1
0	7	1871	11	0.5	0.8	-0.6	6	7	1372	91	3.4	1.7	0.0
0	9	1984	16	1.1	1	-1.0	6	9	989	73	4.1	1.8	-0.3
0	11	1998	24	1.4	1.3	-2.4	6	11	957	86	7	2.7	-0.4
0	13	2614	31	1.2	1.1	-1.5	6	13	935	56	3.3	1.7	-2.5
0	15	2019	29	2	1.4	-0.5	6	15	968	220	8.7	2.7	-1.6
0	17	998	12	0.4	0.7	-0.5	6	17	638	123	3.3	1.9	-1.7
0	19	1000	21	0.2	0.4	-0.9	8	1	1594	30	2.4	1.6	-0.1
2	1	1551	5	0.3	0.6	-2.1	8	3	1021	52	4.2	2.2	-0.1
2	3	918	12	0.5	0.8	-0.1	8	5	1011	74	10.1	3.8	-0.4
2	5	1016	21	1.7	1.2	-0.3	8	7	1018	137	6.1	2.2	-0.5
2	7	1067	13	1.4	1.3	-1.4	8	9	1260	228	10.5	3	-1.5
2	9	994	26	1.9	1.5	0.0	8	11	962	145	10.5	3.1	-0.2
2	11	1051	25	3.1	1.7	-0.4	8	13	1050	254	7.2	2.2	-0.6
2	13	1398	53	2.6	1.6	-0.2	8	15	1334	684	17.6	3.9	-11
2	15	1028	39	3	1.6	-0.5	10	1	2006	33	2.8	1.7	-4.1
2	17	1127	47	2	1.2	-0.4	10	3	980	26	2.7	1.6	-2.3
2	19	1614	144	2	1.3	-0.6	10	5	1051	122	8.9	3	-0.1
4	1	1046	7	0.4	0.8	-0.4	10	7	975	151	4.8	2.5	-0.5
4	3	1697	28	2.3	1.5	-0.6	10	9	1048	287	9.7	3	0.0
4	5	1021	43	3.8	2	-0.4	10	11	982	428	11.1	3.3	-0.3
4	7	1416	42	3.2	1.6	-0.7	10	13†	1039	10	7.7	2.9	
4	9	979	44	3.2	1.7	-0.4	10	15†	854	9	10.9	3.2	
4	11	1456	112	8.8	2.8	-1.1	12	1	1988	106	1.2	1	-0.5
4	13	962	67	4.4	2	-0.3	12	3	904	119	2	1.4	-1.4
4	15	1063	101	8.2	2.8	-0.1	12	5	1032	311	4	2	-6.1
4	17	1062	112	3.6	1.9	-0.3	12	7	2544	31	5.3	2.1	-18
4	19	909	207	2.6	2	-2.4							

These include the number of cycles over which ion counts are accumulated C_{exp}, the number of simultaneous counts n_{sim}, the background level n_{bkgd}, and the background fluctuation δn_{bkgd}. The values for n_{sim}, n_{bkgd}, and δn_{bkgd} are obtained after the momentum-based screening is applied. The coincidence counts for each state-pair are calculated as $n_{coin} = n_{sim} - n_{bkgd}$. Also included are the (base 10) logarithm of the state-specific *P*-values used towards hypothesis testing.

†Energetically forbidden state-pairs.